

## A TURNOVER IN THE GALAXY MAIN SEQUENCE OF STAR FORMATION AT $M_* \sim 10^{10} M_\odot$ FOR REDSHIFTS $z < 1.3$

NICHOLAS LEE<sup>1</sup>, D. B. SANDERS<sup>1</sup>, CAITLIN M. CASEY<sup>1,2</sup>, SUNE TOFT<sup>3</sup>, N. Z. SCOVILLE<sup>4</sup>, CHAO-LING HUNG<sup>1,5</sup>,  
EMERIC LE FLOC'H<sup>6</sup>, OLIVIER ILBERT<sup>7</sup>, H. JABRAN ZAHID<sup>1,5</sup>, HÉRVÉ AUSSEL<sup>6</sup>, PETER CAPAK<sup>4,8</sup>, JEYHAN S. KARTALTEPE<sup>9,14</sup>,  
LISA J. KEWLEY<sup>10</sup>, YANXIA LI<sup>1</sup>, KEVIN SCHAWINSKI<sup>11</sup>, KARTIK SHETH<sup>12</sup>, AND QUANBAO XIAO<sup>1,13</sup>

<sup>1</sup> Institute for Astronomy, 2680 Woodlawn Drive, Honolulu, HI 96822, USA

<sup>2</sup> Department of Physics and Astronomy, University of California, Irvine, CA 92697, USA

<sup>3</sup> Dark Cosmology Centre, Niels Bohr Institute, University of Copenhagen, Juliana Mariesvej 30, DK-2100 Copenhagen, Denmark

<sup>4</sup> California Institute of Technology, MS 105-24, 1200 East California Boulevard, Pasadena, CA 91125, USA

<sup>5</sup> Harvard-Smithsonian Center for Astrophysics, Cambridge, MA 02138, USA

<sup>6</sup> UMR AIM (CEA-UP7-CNRS), CEA-Saclay, Orme des Merisiers, bât. 709, F-91191 Gif-sur-Yvette Cedex, France

<sup>7</sup> Aix Marseille Université, CNRS, LAM (Laboratoire d’Astrophysique de Marseille) UMR 7326, F-13388 Marseille, France

<sup>8</sup> Spitzer Science Center, 314-6 Caltech, 1201 East California Boulevard, Pasadena, CA 91125, USA

<sup>9</sup> National Optical Astronomy Observatory, 950 North Cherry Avenue, Tucson, AZ 85719, USA

<sup>10</sup> Research School of Astrophysics, Australian National University, Canberra, ACT 0200, Australia

<sup>11</sup> Institute for Astronomy, Department of Physics, ETH Zurich, Wolfgang-Pauli-Strasse 27, CH-8093 Zurich, Switzerland

<sup>12</sup> National Radio Astronomy Observatory, 520 Edgemont Road, Charlottesville, VA 22903, USA

<sup>13</sup> The Shanghai Key Lab for Astrophysics, 100 Guilin Road, Shanghai 200234, China

Received 2014 July 29; accepted 2015 January 5; published 2015 March 5

### ABSTRACT

The relationship between galaxy star formation rates (SFRs) and stellar masses ( $M_*$ ) is reexamined using a mass-selected sample of  $\sim 62,000$  star-forming galaxies at  $z \leq 1.3$  in the COSMOS 2 deg<sup>2</sup> field. Using new far-infrared photometry from *Herschel*-PACS and SPIRE and *Spitzer*-MIPS 24  $\mu\text{m}$ , along with derived infrared luminosities from the NRK method based on galaxies’ locations in the restframe color–color diagram (NUV –  $r$ ) versus ( $r$  –  $K$ ), we are able to more accurately determine total SFRs for our complete sample. At all redshifts, the relationship between median SFR and  $M_*$  follows a power law at low stellar masses, and flattens to nearly constant SFR at high stellar masses. We describe a new parameterization that provides the best fit to the main sequence and characterizes the low mass power-law slope, turnover mass, and overall scaling. The turnover in the main sequence occurs at a characteristic mass of about  $M_0 \sim 10^{10} M_\odot$  at all redshifts. The low mass power-law slope ranges from 0.9–1.3 and the overall scaling rises in SFR as a function of  $(1+z)^{4.12 \pm 0.10}$ . A broken power-law fit below and above the turnover mass gives relationships of  $\text{SFR} \propto M_*^{0.88 \pm 0.06}$  below the turnover mass and  $\text{SFR} \propto M_*^{0.27 \pm 0.04}$  above the turnover mass. Galaxies more massive than  $M_* \gtrsim 10^{10} M_\odot$  have a much lower average specific star formation rate (sSFR) than would be expected by simply extrapolating the traditional linear fit to the main sequence found for less massive galaxies.

**Key words:** galaxies: evolution – galaxies: high-redshift – galaxies: star formation

### 1. INTRODUCTION

Over the last decade, a tight correlation between a galaxy’s star formation rate (SFR) and its stellar mass ( $M_*$ ) has been discovered (Noeske et al. 2007; Daddi et al. 2007; Elbaz et al. 2007; Salim et al. 2007). Commonly referred to as the galaxy “main sequence” (MS) of star formation, this relationship has important implications for the physical nature of star formation in galaxies. The MS is generally described as a single power law of the form  $\text{SFR} \propto M_*^\beta$ , with  $\beta = 0.7$ –1.0 and the normalization of the MS evolving to higher values at increasing redshift (Noeske et al. 2007).

A common interpretation of the existence and tightness of the MS is that the majority of star-forming galaxies are powered by similar quasi-steady processes, with only a small fraction of galaxies undergoing more chaotic processes such as major merger events that might be expected to produce strong bursts of star formation (e.g., Elbaz et al. 2011; Rodighiero et al. 2011; Sargent et al. 2012). These starburst galaxies are generally thought to lie significantly above the MS and represent a minority of galaxies.

A key uncertainty in measuring galaxy SFRs is the effect of dust obscuration. The most direct method of determining dust obscuration is from observations in the far-infrared, where the absorbed starlight is thermally reradiated. In the absence of far-infrared data, various extrapolations from shorter wavelength have been used to study the MS, such as using emission lines combined with reddening corrections to infer the dust-corrected SFR (Brusa et al. 2010; Sobral et al. 2012; Zahid et al. 2012; Kashino et al. 2013) or measuring the UV or optical emission from young massive stars and correcting for the radiation lost to dust obscuration (Lee et al. 2011; Rodighiero et al. 2011; Steinhardt et al. 2014). Observations in the mid-infrared (e.g., 24  $\mu\text{m}$ ) have been used to estimate far-infrared luminosities (e.g., Noeske et al. 2007; Daddi et al. 2007; Elbaz et al. 2007), although the accuracy of these estimates decreases at high redshifts and bright infrared luminosities (e.g., Papovich et al. 2007; Lee et al. 2010; Elbaz et al. 2011). Studies of radio emission take advantage of the well-known radio–FIR correlation (Helou et al. 1985; Condon 1992; Yun et al. 2001) to estimate the infrared luminosities, but many of these studies rely on stacking to overcome high sensitivity limits (Dunne et al. 2009; Pannella et al. 2009; Karim et al. 2011). The consensus from these studies is that the MS follows a single power law

<sup>14</sup> Hubble Fellow.

$SFR \propto M_*^\beta$ , with the slope generally between  $\beta = 0.7\text{--}1.0$  and the normalization varying based on the study’s redshift, SFR indicator, sample selection, and initial mass function (IMF; for a summary, see Speagle et al. 2014).

However, a few studies have found indications of a more complex MS relationship. Some studies suggest that the MS slope varies with stellar mass so that a single power law cannot explain the MS and a stellar mass-dependent slope is a better fit (Karim et al. 2011; Whitaker et al. 2012; Magnelli et al. 2014). Recent studies based on far-infrared selected samples from *Herschel* show that far-infrared selected galaxies lie mostly above the MS, with a much shallower slope in  $\log(SFR)/\log(M_*)$  (Lee et al. 2013; Oteo et al. 2013a, 2013b; Lemaux et al. 2014). However, this discrepancy is due to the flux limited selection of far-infrared samples that introduce a SFR-based selection bias, as compared to studies based on stellar mass-selected galaxy samples. This has been demonstrated by stacking analyses that explore the far-infrared emission as a function of stellar mass and find generally good agreement between dust-corrected UV-derived SFRs and *Herschel*-derived SFRs (e.g., Rodighiero et al. 2014).

Stacking is a commonly used technique to measure low-level emission from galaxies that would be undetected individually. Stacking analyses require a number of assumptions and can miss vital information about individual galaxies and their distributions. Unless the parent population is identical (a key assumption in stacking), interpretation of stacking results can be difficult because the underlying distribution is unknown (although see Schreiber et al. 2014, for a possible method to determine the underlying distribution). In addition, these stacking analyses do not explain why the dust-corrected SFRs cannot accurately recover the SFRs seen in high luminosity galaxies, which have an elevated contribution to the integrated build up of stellar mass in the universe.

Direct *Herschel* FIR measurements remain a unique tool to properly estimate the ongoing star formation rate in the most active dusty galaxies. Analysis of the rest-frame UV emission in dusty galaxies suggests that applying the nominal attenuation laws (e.g., Meurer et al. 1999; Calzetti et al. 2000) will dramatically underestimate total star formation rate in galaxies exceeding  $\sim 50 M_\odot \text{ yr}^{-1}$  (Smail et al. 2004; Casey et al. 2014; Rodighiero et al. 2014).

In the following paper, we attempt to address these issues by using a dust-corrected SFR indicator that is accurate for galaxies at all luminosities. By analyzing a large sample of individual galaxies, we do not lose information about the distribution of sources from stacking and can re-examine the shape of the star-forming MS in a stellar mass-selected sample. The data are described in Section 2 and SFRs computed by several different methods are measured and compared in Section 3. In Section 4 we analyze our mass-selected sample of galaxies in the  $SFR/M_*$  plane and find the best fits to the data. The implications of the MS are discussed in Section 5 and we list our conclusions in Section 6. When calculating rest-frame quantities, we use a cosmology with  $\Omega_m = 0.28$ ,  $\Lambda = 0.72$ , and  $H_0 = 70 \text{ km s}^{-1} \text{ Mpc}^{-1}$  (Hinshaw et al. 2013). A Chabrier (2003) IMF truncated at 0.1 and  $100 M_\odot$  is used when deriving SFRs and stellar masses.

## 2. DATA

Our analysis of the MS is made possible by the large area multi-wavelength coverage of the COSMOS field, a  $2 \text{ deg}^2$  area

of the sky with observations from the ultraviolet through far-infrared and radio (Scoville et al. 2007). We construct a mass-complete sample of galaxies with  $K_s < 24$  from the deep  $K_s$ -band catalog of Ilbert et al. (2013), based on data from the first UltraVISTA DR1 data release, covering  $\sim 75\%$  of the COSMOS field (McCracken et al. 2012). Twenty bands of optical and near-infrared photometry were extracted using matched apertures in dual-image mode from the various available COSMOS images and was combined with *GALEX* magnitudes from the multi-wavelength catalog of Capak et al. (2007). We use updated *Spitzer* IRAC photometry from the Spitzer Large Area Survey with Hyper-Suprime-CAM (SPLASH; Steinhardt et al. 2014). We cross-match this catalog with the *Spitzer* MIPS  $24 \mu\text{m}$  catalog of Le Floc’h et al. (2009) and the *Herschel* catalog of Lee et al. (2013) using a matching radius of  $2''$ .

### 2.1. Source Selection

We interpolate the 90% stellar mass completeness limits from Ilbert et al. (2013) to determine approximate mass completeness thresholds at all redshifts, and select only galaxies with stellar masses above their redshift dependent mass completeness limit. When studying star-forming galaxy populations, we separate “star-forming” and “quiescent” galaxies using a modified version of the Williams et al. (2009) two-color selection technique:  $\text{NUV} - r^+$  versus  $r^+ - J$  (as described in Ilbert et al. 2013). Specifically, galaxies with absolute magnitude colors  $M_{\text{NUV}} - M_r > 3(M_r - M_J) + 1$  and  $M_{\text{NUV}} - M_r > 3.1$  are considered “quiescent” ( $\sim 15\%$  of the sample) while the remaining galaxies are considered actively star-forming galaxies.

Star-forming galaxies that also contain luminous active galactic nuclei (AGNs) are a concern because the luminosity from the AGN is extremely difficult to separate from emission from star formation, and thus these sources may have erroneously high SFRs (although this concern is lessened for FIR sources because AGNs generally heat dust to temperatures too hot to radiate in the far-infrared). On the other hand, many of the galaxies that host AGNs also contain significant star formation, and removing these sources introduces a bias to our study. We find that the overall results of our study are not significantly affected by either the inclusion or exclusion of these sources, so we do not remove galaxies that have been detected in the X-ray ( $\sim 0.5\%$  of sample) by *XMM-Newton* (Brusa et al. 2010) or *Chandra* (Civano et al. 2011), or that have IRAC power-law colors (Donley et al. 2008) that suggest AGN activity ( $\sim 25\%$  of sample).

### 2.2. Infrared Data

The *Herschel*-selected sample of galaxies is described in detail in Lee et al. (2013, hereafter L13) and is briefly summarized here. L13 use *Spitzer*  $24 \mu\text{m}$  and VLA 1.4 GHz priors to find 4,218 sources in COSMOS that were each detected in at least two of the five available *Herschel* PACS ( $100 \mu\text{m}$  or  $160 \mu\text{m}$ ) and SPIRE ( $250 \mu\text{m}$ ,  $350 \mu\text{m}$ , or  $500 \mu\text{m}$ ) bands. These sources span  $\log(L_{\text{IR}}/L_\odot) = 9.4\text{--}13.6$  and  $z = 0.02\text{--}3.54$ . Dust properties of each source (e.g.,  $L_{\text{IR}}$ ,  $T_{\text{dust}}$ ,  $M_{\text{dust}}$ ) were measured by fitting the full infrared photometry to a coupled modified blackbody plus mid-infrared power law using the prescription given in Casey (2012) and assuming an opacity model where  $\tau = 1$  at  $200 \mu\text{m}$ .

There is a population of galaxies that are classified as “quiescent” from their  $\text{NUV} - r^+$  versus  $r^+ - J$  colors, but have been detected in the infrared by *Herschel* or *Spitzer*, suggesting that these galaxies are actually undergoing a significant amount

of star formation ( $\sim 7\%$  of the “quiescent” population). These galaxies are more consistent with being very dusty objects that have extremely red colors due to obscuration, not lack of active star formation, so we include these galaxies in our sample of star-forming galaxies (see Section 4.3).

### 2.3. Photometric Redshifts and Physical Parameters

Ilbert et al. (2013) measure accurate 30 band photometric redshifts of the full  $K_s$ -band COSMOS catalog. We find a median  $\Delta z/(1+z) = 0.02$  in our sample of star-forming galaxies, with a catastrophic failure ( $|\Delta z|/(1+z) > 0.15$ ) in 5.6% of sources. In addition, physical parameters such as stellar mass and star formation rate have been calculated by fitting the spectral energy distributions (SEDs) to synthetic spectra generated using the stellar population synthesis (SPS) models of Bruzual & Charlot (2003). We also recalculate the physical parameters using different templates and extraction parameters, and find that our final results are not affected by the specific choice of template. Thus, we use the same set of parameters used to create the catalog in Ilbert et al. (2013), but with updated near-IR photometry from SPLASH.

## 3. ANALYSIS

### 3.1. Star Formation Rate Calculations

There are many methods for estimating a galaxy’s SFR based on observations at various wavelengths (for a review, see Kennicutt 1998; Murphy et al. 2011). Here we compare a few commonly used SFR indicators using a subset of COSMOS galaxies to determine how much the different SFR methods disagree. In all cases, we measure the total SFR as  $SFR_{\text{tot}} = SFR_{\text{IR}} + SFR_{\text{UV}}$ .

#### 3.1.1. Infrared Derived SFR

As discussed in Section 2.2, the infrared properties of the *Herschel*-selected galaxies have been measured by fitting the infrared SEDs to a coupled modified blackbody plus mid-infrared power-law model (Casey 2012). It has been shown that measuring the  $L_{\text{IR}}$  from fitting the far-infrared data to libraries of SED (e.g., Chary & Elbaz 2001; Dale & Helou 2002) gives roughly the same results as the modified blackbody plus power-law model (Casey 2012; U et al. 2012; Lee et al. 2013). The infrared observations give us an estimate of the obscured SFR, and we combine this with UV observations of the unobscured SFR to derive the total SFR as in Arnouts et al. (2013):

$$SFR_{\text{Total}} = (8.6 \times 10^{-11}) \times (L_{\text{IR}} + 2.3 \times \nu L_{\nu}(2300 \text{ \AA})) \quad (1)$$

where  $L_{\text{IR}} \equiv L(8\text{--}1000 \mu\text{m})$  and all luminosities are measured in units of  $L_{\odot}$ . For sources with  $SFR \gtrsim 50 M_{\odot} \text{ yr}^{-1}$ , the infrared contribution dominates the total SFR, contributing as much as  $\sim 90\%$  of the total SFR.

While we have excellent *Herschel* coverage of the full 2 deg $^2$  COSMOS field that yields 4218 sources, the detection limits of *Herschel* introduce a selection bias against all but the most luminous infrared sources. A common method of determining the  $L_{\text{IR}}$  of less luminous galaxies is to use deep *Spitzer* 24  $\mu\text{m}$  data to estimate the far-infrared luminosity (e.g., Kennicutt et al. 2009; Rieke et al. 2009; Rujopakarn et al. 2013). COSMOS has extremely deep coverage at 24  $\mu\text{m}$  and Le Floc’h et al. (2009) provide SFR estimates for 36,635 galaxies, which we use to extend our sample of infrared detected galaxies to more moderate luminosities.

### 3.1.2. Optical- and UV-based SFR Indicators

For galaxies without direct measurements from far- or mid-infrared wavelengths of the obscured SFR, the amount of radiation obscured by dust must be estimated indirectly. A common method for estimating total SFR is to fit libraries of model SEDs (that include prescriptions for dust obscuration) to optical and UV photometry and fit to a library of synthetic spectra from Bruzual & Charlot (2003), and estimate the total SFR for each of the galaxies in our sample from the best fit SEDs.

Another method of estimating dust-corrected SFRs is by using rest-frame UV observations to measure the unobscured SFR and inferring the appropriate dust correction factor from observed colors. Two examples of this are the  $BzK$  method from Daddi et al. (2004) and the NRK method from Arnouts et al. (2013).  $BzK$  SFRs are determined by using the observed-frame  $B$ -band photometry to measure the rest-frame UV luminosity, and then estimating the extinction as  $E(B-V) = 0.25(B-z+0.1)_{\text{AB}}$  (Daddi et al. 2007).  $BzK$  SFRs are only valid for redshifts  $1.4 < z < 2.5$ , as these are the only redshifts where the desired portions of the SED are redshifted to the correct wavelengths, and we limit our selection to the *good-sBzK* with errors  $\delta \log[\text{SFR}(\text{UV})] < 0.3$  dex (Rodighiero et al. 2014).

NRK SFRs are calculated by using their location in the rest-frame color-color diagram ( $\text{NUV}-r$ ) versus  $(r-K)$  to estimate extinction. Arnouts et al. (2013) find that at  $z \lesssim 1.3$ , the infrared excess  $\text{IRX} \equiv L_{\text{IR}}/L_{\text{NUV}}$  in star-forming galaxies can be parameterized as a function of redshift and the vector  $\text{NRK} = 0.31 \times (\text{NUV}-r) + 0.95 \times (r-K)$ . This allows us to estimate the  $L_{\text{IR}}$  and calculate total SFR using Equation (1). When measuring NRK SFRs, we use the small “sSFR correction” as described in Arnouts et al. (2013).

### 3.2. Comparison of SFR Indicators

We compare commonly used SFR indicators using a common subset of COSMOS galaxies to determine how much agreement there is between the different measures of SFR. We have a large set of *Herschel* detected galaxies from Lee et al. (2013) where, for the first time, we have direct measurements of both the obscured and unobscured SFR (from UV observations) at a wide range of redshifts. We compare the other SFR indicators discussed previously (24  $\mu\text{m}$ , SED fits,  $BzK$ , and NRK) to this sample of 4218 *Herschel* detected galaxies.

Figure 1 displays the comparison of  $SFR_{\text{Total}}$  from the four different indicators discussed above to  $SFR_{\text{Total}}$  as measured by *Herschel*. Density contours show the location and concentration of the majority of the sources, with outliers shown in gray circles. Median values in 20 equally populated bins of  $SFR_{\text{Total},\text{Herschel}}$  are overplotted to show average trends. To determine the strength of the correlation between each SFR indicator and  $SFR_{\text{Total},\text{Herschel}}$ , we measure the Pearson correlation coefficient ( $\rho$ ) and provide these values at the top of each subplot. The Pearson correlation coefficient can vary between +1 and -1, with +1 indicating total positive correlation, 0 indicating no correlation, and -1 indicating total negative correlation. We also measure the median difference between each SFR indicator and *Herschel* SFR ( $\langle \Delta \log(\text{SFR}) \rangle$ ) and list these values at the top of each subplot.

The 24  $\mu\text{m}$  determined SFR correlates with the *Herschel* SFR very well ( $\rho_{24} = 0.88$ ,  $\langle \Delta \log(\text{SFR}_{24}) \rangle = 0.12$ ), except at the highest IR luminosities. This trend has been previously explored

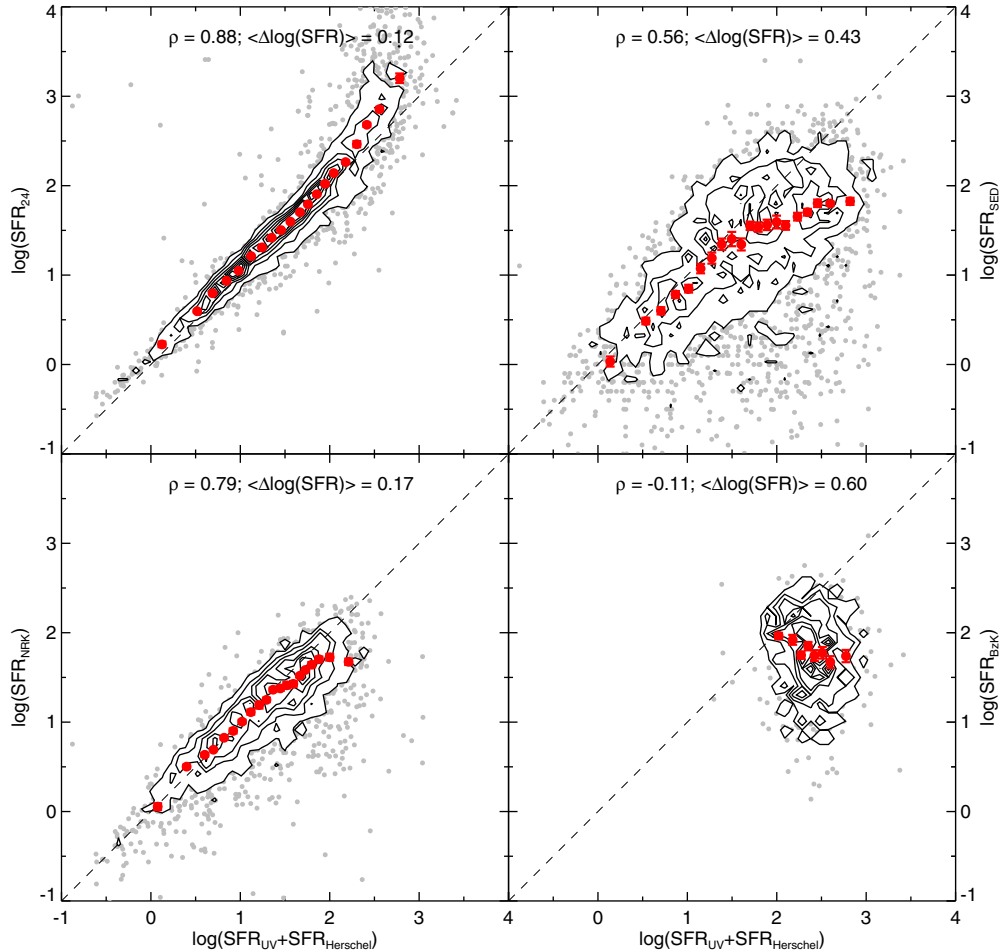


**Figure 1.** Comparison of total SFR determined from combining direct measurements of FIR (*Herschel*; Lee et al. 2013) and UV (*GALEX*; Zamojski et al. 2007) with various SFR indicators using observations at shorter wavelengths. The different SFR indicators are: (top left) *Spitzer* 24  $\mu\text{m}$  (Le Floc'h et al. 2009) + *GALEX*; (top right) multi-wavelength SED fits (Ilbert et al. 2013); (bottom left) NRK ( $0 < z < 1.3$ , Arnouts et al. 2013); and (bottom right) BzK ( $1.4 < z < 2.5$ , Daddi et al. 2007). In each panel, black contours give the density and concentration of sources, with extreme outliers plotted as gray circles. We bin the data in 20 equally populated bins (except BzK, which has 8 bins) and find the median SFR<sub>indicator</sub> in each bin. Errors on the median points are measured using a bootstrapping technique and are plotted when larger than the size of the symbol. At the top of each panel is the Pearson correlation coefficient (with a value of +1 indicating strong positive correlation and 0 indicating no correlation) and the typical difference between each particular SFR indicator and the *Herschel*-derived SFR.

in many studies which find that at moderate redshifts and IR luminosities, 24  $\mu\text{m}$  observations are a good proxy for  $L_{\text{IR}}$ , but at high redshifts and infrared luminosities, the 24  $\mu\text{m}$  estimates tend to overpredict the true  $L_{\text{IR}}$ , possibly due to redshifting of the observed 24  $\mu\text{m}$  band to wavelengths contaminated by polycyclic aromatic hydrocarbon features (e.g., Papovich et al. 2007; Lee et al. 2010; Elbaz et al. 2011). As we are using the 24  $\mu\text{m}$  SFRs to fill in the low and moderate luminosity galaxies that are not detected with *Herschel*, this discrepancy is not a major issue for our work.

The NRK SFRs also show strong correlation with the *Herschel*-derived SFRs ( $\rho_{\text{NRK}} = 0.79$ ,  $\langle \Delta \log(\text{SFR}_{\text{NRK}}) \rangle = 0.17$ ). This is not completely unexpected since the NRK method was developed using 24  $\mu\text{m}$  derived SFRs as a baseline, but the NRK measured SFRs match very well with those derived from *Herschel*. Like with SFR<sub>24</sub>, the correlation shows signs of breaking down at the highest SFRs, but as long as the NRK is used mainly for low SFR galaxies, it provides a reliable estimate of the SFR.

By contrast, the agreement between SFR<sub>SED</sub> and SFR<sub>Total</sub> is quite poor, showing much weaker correlation between the two indicators ( $\rho_{\text{SED}} = 0.56$ ). The tightness of the correlation is also much broader ( $\langle \Delta \log(\text{SFR}_{\text{SED}}) \rangle = 0.43$ ), even at low SFRs

where the median points lie closer to the unity line. Again, at high SFRs the median points show a clear deviation from unity. Wuyts et al. (2011) are able to find a better match between SFR<sub>SED</sub> and SFR<sub>24</sub> if they tune key parameters of the SED fit, such as  $\tau_{\min}$ , the  $e$ -folding time of the exponentially declining star formation history. The exact tuning needed varies based on several other assumptions in the SED fitting procedure, such as different stellar population synthesis codes, and even when the tuning is done, the computed SFR<sub>SED</sub> still systematically underestimates the true SFR for a significant fraction of sources.

Finally, the comparison between SFR<sub>BzK</sub> and SFR<sub>Total</sub> shows essentially no correlation ( $\rho_{\text{BzK}} = -0.11$ ). It should be noted that the redshift range of the BzK indicator ( $1.4 < z < 2.5$ ) limits us to a small sample size containing only the brightest galaxies. As seen in Figure 2, this selection limits our comparison to galaxies at SFRs where all indicators begin to deviate significantly from SFR<sub>Total</sub>. Stacking analyses suggest a stronger correlation between average SFR<sub>BzK</sub> and average SFR<sub>Herschel</sub> at fainter luminosities (Rodighiero et al. 2014), but the tightness of the distribution is not well determined. The BzK galaxies that are *Herschel* detected show no correlation between the SFR derived from the BzK method and from *Herschel* measurements.

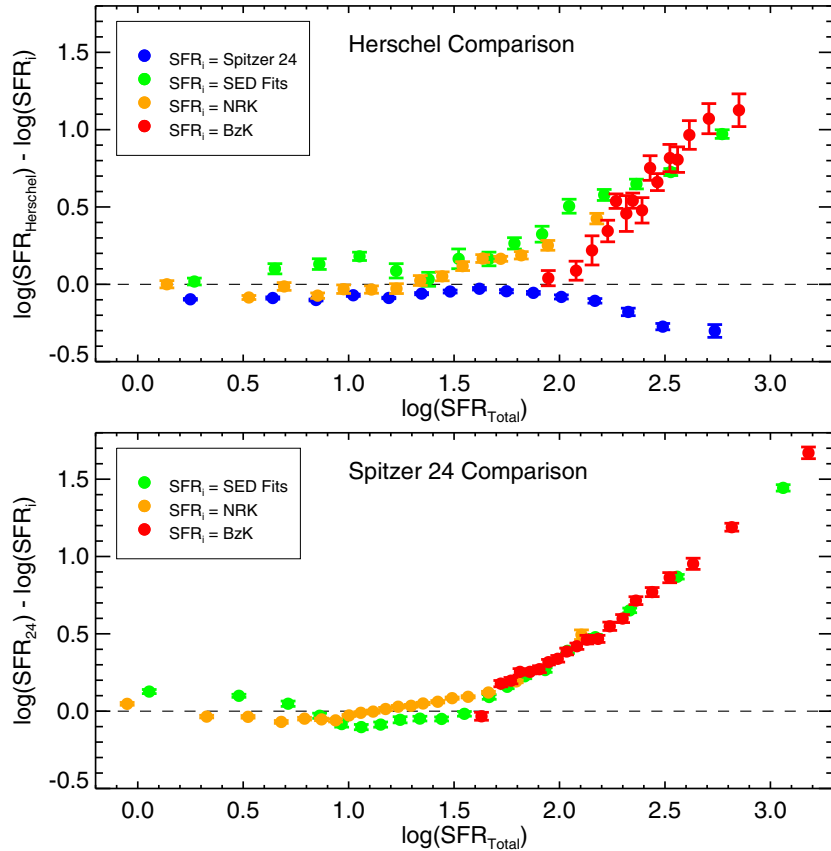


**Figure 2.** Median difference in SFR estimated from infrared vs. optical/UV indicators, as a function of total SFR. Sources that were detected by both SFR indicators were split in 15 equally populated  $\log(\text{SFR}_{\text{Total}})$  bins, and the median value is plotted, with error bars representing bootstrapped errors. We see that all indicators begin to deviate significantly at  $\log(\text{SFR}) \gtrsim 1.5$ . (Top) Comparison of *Spitzer* 24  $\mu\text{m}$  + *GALEX* (blue), multi-wavelength SED fits (green), NRK (orange,  $0 < z < 1.3$ ), and *BzK* (red,  $1.4 < z < 2.5$ ) to total SFR as derived from *Herschel*. (Bottom) Comparison of multi-wavelength SED fits (green), NRK (orange,  $0 < z < 1.3$ ), and *BzK* (red,  $1.4 < z < 2.5$ ) to total SFR as derived from *Spitzer* 24  $\mu\text{m}$ .

### 3.2.1. Selection Effects of SFR Indicators

The comparisons of the various SFR indicators shown in Figure 1 span different dynamic ranges in SFR, mostly due to the redshift limitations of the NRK and *BzK* indicators. In Figure 2, we plot the typical difference between SFR indicators and  $\text{SFR}_{\text{Total}}$  as a function of  $\log(\text{SFR}_{\text{Total}})$ . We see that all of the SFR indicators provide poor estimates of the infrared measured  $\text{SFR}_{\text{Total}}$  above  $\log(\text{SFR}) \gtrsim 1.5$  ( $\sim 30 M_{\odot} \text{ yr}^{-1}$ ). These common SFR indicators fail to accurately estimate the true SFR of luminous infrared galaxies. This highlights the need for direct infrared observations to accurately measure the SFR of highly star forming galaxies.

Throughout this analysis we have assumed the *Herschel*-determined SFR is the most accurate because it directly probes far-infrared wavelengths, where the bulk of the re-radiated radiation from dust is emitted. However, it is possible that the high detection threshold of *Herschel* limits us to a biased sample that does not accurately reflect the emission properties of lower luminosity galaxies. To test this possibility, we re-run our analyses using the much deeper sample of *Spitzer* 24  $\mu\text{m}$  detected galaxies (which showed excellent agreement with *Herschel* SFRs) as the comparison sample. We find very similar results as the *Herschel* comparison, with NRK providing both the strongest correlation and the tightest distribution.

### 3.2.2. A Ladder of SFR Indicators

While all three non-infrared based SFR indicators fail to accurately estimate the SFR in high luminosity galaxies, the

NRK method provides the most accurate and consistent estimates across the full dynamical range of *Herschel* SFRs. At high SFRs ( $\text{SFR} \gtrsim 30 M_{\odot} \text{ yr}^{-1}$ ), 70% of our sample is directly detected in the infrared by either *Herschel* or *Spitzer*. Thus, we can study the full population of star forming galaxies by constructing a “ladder” of SFR indicators (as in Wuyts et al. 2011) based on the *Herschel*, *Spitzer* 24  $\mu\text{m}$ , and NRK SFR indicators. All sources have  $\text{SFR}_{\text{Total}}$  calculated using Equation (1), with different methods of determining  $L_{\text{IR}}$ . For sources detected by *Herschel*, we measure  $L_{\text{IR}}$  from fitting the far-infrared photometry to the Casey (2012) graybody plus power-law models. We use the  $L_{\text{IR}}$  estimated from 24  $\mu\text{m}$  (Le Floc'h et al. 2009) for sources that are not detected by *Herschel* but are detected at *Spitzer* 24  $\mu\text{m}$ . And for the remaining sources, we estimate  $L_{\text{IR}}$  using the NRK-derived IRX (as discussed in Section 3.1.2). Although we include NRK-derived IRX for all galaxies above our mass-completeness limits, the method has only been well-calibrated for  $M_* > 10^{9.3} M_{\odot}$ . Infrared stacking suggests that any systematic offsets should be small, but when calculating MS relationships we only include galaxies with  $M_* > 10^{9.3} M_{\odot}$ .

The relative fraction of sources with SFRs measured from each indicator is plotted in Figure 3 as a function of both stellar mass and redshift. Below  $M_* \lesssim 10^{9.5} M_{\odot}$ , SFRs are almost all determined from NRK, but at higher stellar masses, the fraction of sources with direct infrared measurements increases until about 25% (60%) of sources at  $M \gtrsim 10^{10.5} M_{\odot}$  have SFRs determined from *Herschel* (*Spitzer* 24  $\mu\text{m}$ ). Because of the redshift limitations of the NRK method (see Arnouts et al. 2013) and the larger errors associated with the  $\text{SFR}_{\text{SED}}$  and

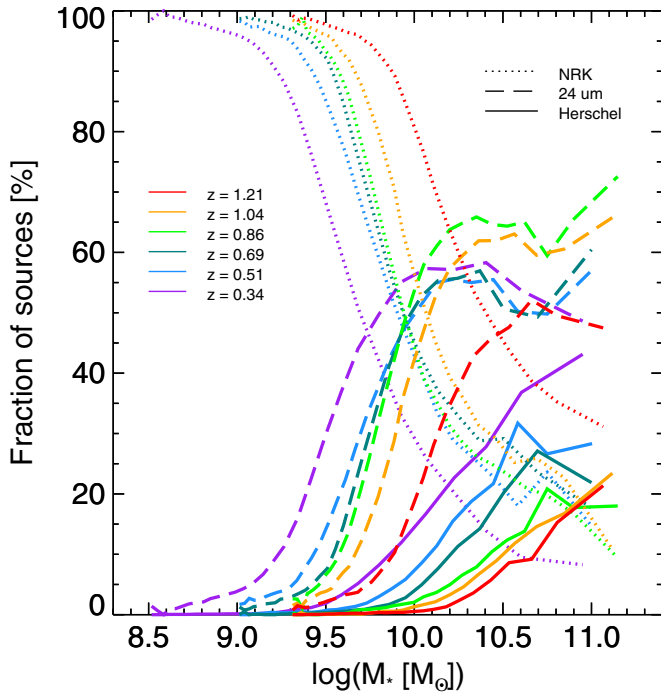


**Figure 3.** Relative fraction of sources with SFRs determined from NRK (dotted line), *Spitzer* 24  $\mu\text{m}$  (dashed line), and *Herschel* (solid line). Different colored lines represent percentages in different redshift bins, with bluer colors representing low redshifts and redder colors representing high redshifts.

SFR<sub>BZK</sub> indicators, we restrict the rest of our analysis to redshifts  $0 < z < 1.3$ , where we can more accurately measure the SFR of our full sample.

#### 4. SHAPE OF THE MAIN SEQUENCE OF STAR FORMATION

With reliable and consistent SFR estimates for a large, mass-complete sample of galaxies in COSMOS, we examine the star-forming MS for a large, unbiased sample of 62,521 galaxies. Figure 4 displays the stellar mass and SFR of our full sample, split into four redshift bins spanning  $0.2 \leq z \leq 1.3$ . Black contours display the density of sources at each location in SFR and  $M_*$  parameter space, and colored bars represent the median SFR in stellar mass bins of width  $\Delta \log(M_*) = 0.3$ , with vertical error bars displaying the standard deviation of the SFRs in that bin. These same bins are used to create the fractional histograms plotted on the side of each redshift bin, which display the distribution of SFRs within each mass bin with the corresponding color. The derived MS relationships from star-forming galaxies in Karim et al. (2011) and Whitaker et al. (2014) are also plotted for comparison.

Figure 4 shows that the galaxies in our sample do not follow a simple linear MS relationship between  $\log(\text{SFR})$  and  $\log(M_*)$  (or a single power-law relationship between SFR and  $M_*$ ). Instead, the median SFR relationship appears to flatten at masses above  $M_* \sim 10^{10} M_\odot$ . This can be seen in the histograms, which show that the peak of each SFR distribution increases with increasing  $M_*$  at low masses, but at high masses, the histogram peaks all lie at approximately the same SFR. The standard deviation of the SFR in each stellar mass bin remains mostly constant at all masses and at all redshifts, with  $\sigma \sim 0.36$  dex in all bins. The shape of this relationship appears roughly constant with redshift, with the entire relationship increasing to higher SFRs at higher redshifts.

#### 4.1. Parameterizing the Star-forming Main Sequence

From Figure 4, it is clear that a single power law does not accurately describe the relationship between stellar mass and star formation rate. We split our sample of star-forming galaxies into six equally populated redshift bins, each of which are then split into 30 equally populated stellar mass bins (with  $\sim 350$  sources in each bin), and calculate the median SFR in each bin. We limit our sample to stellar masses above a conservative mass limit (see Table 1) to ensure that we are not affected by systematics. The specific number of redshift bins does not affect the following results, although we must balance between having redshift bins that are too wide and combine galaxy samples at different epochs with having redshift bins that are too narrow and are affected by small number statistics. The same is true for the number of stellar mass bins, although having at least 30 bins is preferable for accurately determining the goodness of fit to the models. The median SFRs for every bin are plotted in Figure 5, colored by redshift, with bootstrapped errors on the median represented by vertical bars.

Using the *MPFIT* package implemented in IDL (Markwardt 2009), we fit the median  $\log(M_*)$  and  $\log(\text{SFR})$  in each redshift bin with many models including linear, second order polynomial, and broken linear, and find the best fit is provided by the following model:

$$S = S_0 - \log \left[ 1 + \left( \frac{10^M}{10^{M_0}} \right)^{-\gamma} \right] \quad (2)$$

where  $S = \log(\text{SFR})$  and  $M = \log(M_*/M_\odot)$ . We choose this model because (1) at all redshifts, it provides the best reduced  $\chi^2$  fit to the data, and (2) unlike polynomial fits, the parameters of the model allow us to quantify the interesting characteristics of the relation between stellar mass and SFR:  $\gamma$ , the power-law slope at low stellar masses,  $M_0$ , the turnover mass (in  $\log(M_*/M_\odot)$ ), and  $S_0$ , the maximum value of  $S$  (or the maximum value of  $\log(\text{SFR})$ ) that the function asymptotically approaches at high stellar mass. The best-fit parameters for each redshift bin are listed in Table 1.

#### 4.2. Evolution of Model Parameters

In the top panels of Figure 6, we plot the evolution of  $S_0$ ,  $M_0$ , and  $\gamma$  as functions of  $\log(1+z)$ . The bottom panels of Figure 6 examine the covariance between these parameters by displaying the 95% confidence error ellipses.

We see clear and strong evolution of  $S_0$  with redshift, and the best fit line suggests an evolution of  $S_0 \propto (4.12 \pm 0.10) \times \log(1+z)$ , or equivalently,  $\text{SFR}_0 \propto (1+z)^{4.12 \pm 0.10}$ . The covariance between  $S_0$  and  $M_0$  (Figure 6(D)) and between  $S_0$  and  $\gamma$  (Figure 6(E)) is relatively minor, so we infer that the evolution in  $S_0$  is true evolution and not due to variation in the other parameters.

Both  $M_0$  and  $\gamma$  show some evidence for weak evolution to more massive  $M_0$  and steeper  $\gamma$  with redshift, although much of the perceived evolution may be due to the covariance seen in Figure 6(F). The best (linear) fit to the evolution in the turnover mass is given by  $M_0 \propto (1.41 \pm 0.20) \times \log(1+z)$ . We test the possible redshift evolution of turnover mass by calculating where the data deviates by 0.2 dex from a single power law fit to the low mass data and find similar evolution, suggesting that the turnover mass does indeed change with cosmic time. The low-mass power-law slope,  $\gamma$ , has a best-fit line that suggests evolution of  $\gamma \propto (1.17 \pm 0.13) \times \log(1+z)$ . Redshift evolution

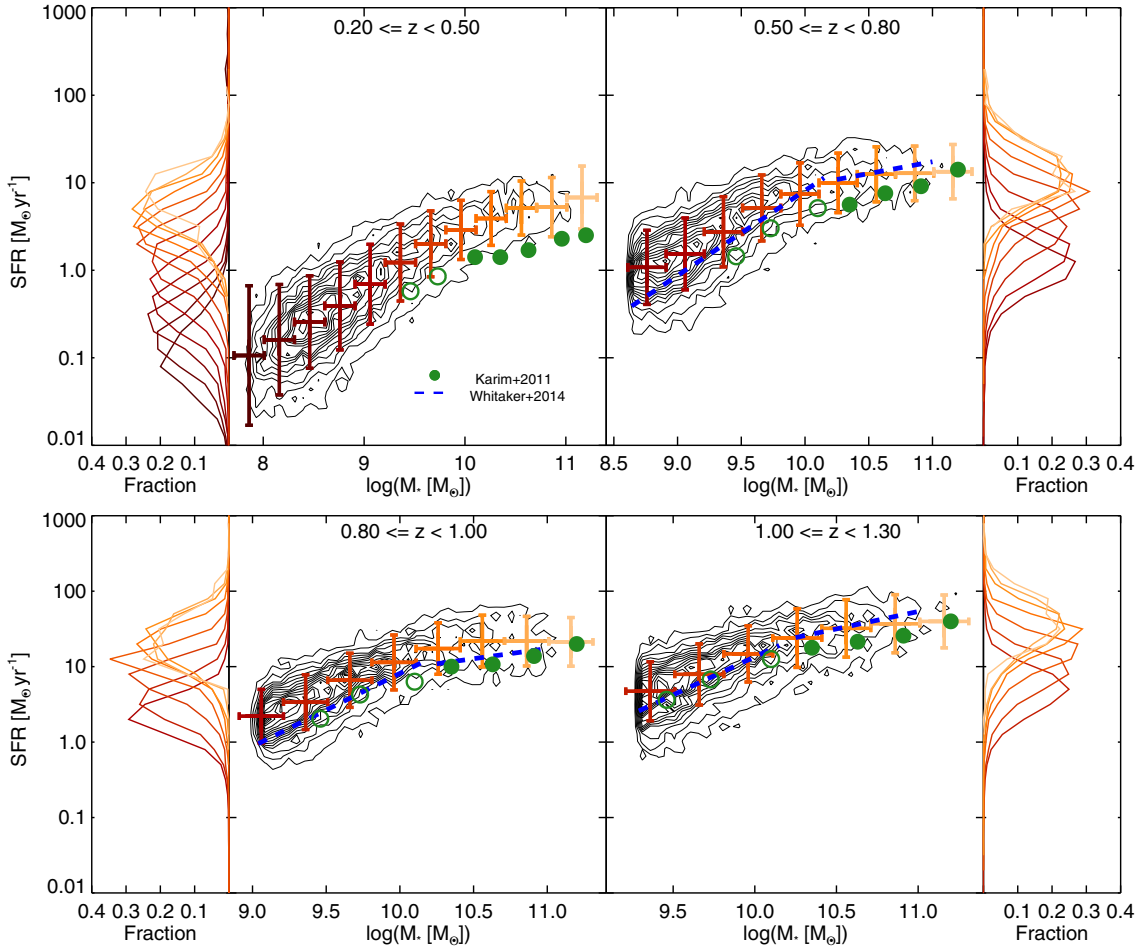


**Figure 4.** Contour density plot of star-forming galaxies in the COSMOS field. We remove all galaxies classified as “quiescent” (unless they were detected in the infrared) and combine all star-forming galaxies, regardless of the specific SFR indicator used. To display the density of sources in the  $SFR/M_*$  plane, each redshift slice was made into a grid of  $51 \times 51$  bins, and the number of sources in each bin was calculated. Black contours show the density of galaxies, with contour levels set at one-half of the standard deviation of the number of sources in each bin. Colored vertical bars represent the median SFR in mass bins of width 0.3 dex and display the overall trend of the  $SFR/M_*$  relationship. Histograms of matching color display the distribution of SFR in each mass bin along the sides of each plot. Main-sequence relationships from Karim et al. (2011, green dots) and Whitaker et al. (2014, blue line) are plotted for comparison.

**Table 1**  
Best-fit Parameters for  $SFR/M_*$  Correlation

Redshift Range	$\langle z \rangle$	$\log(M_{\text{limit}})$ $\log(M_\odot)$	$S_0$ $\log(M_\odot \text{ yr}^{-1})$	$M_0$ $\log(M_\odot)$	$\gamma$	Reduced $\chi^2$
0.25–0.46	0.36	8.50	$0.80 \pm 0.019$	$10.03 \pm 0.042$	$0.92 \pm 0.017$	1.74
0.46–0.63	0.55	9.00	$0.99 \pm 0.015$	$9.82 \pm 0.031$	$1.13 \pm 0.033$	1.52
0.63–0.78	0.70	9.00	$1.23 \pm 0.016$	$9.93 \pm 0.031$	$1.11 \pm 0.025$	1.48
0.78–0.93	0.85	9.30	$1.35 \pm 0.014$	$9.96 \pm 0.025$	$1.28 \pm 0.034$	1.84
0.93–1.11	0.99	9.30	$1.53 \pm 0.017$	$10.10 \pm 0.029$	$1.26 \pm 0.032$	0.62
1.11–1.30	1.19	9.30	$1.72 \pm 0.024$	$10.31 \pm 0.043$	$1.07 \pm 0.028$	1.24

**Notes.** Parameters of the best-fit model to the star-forming main sequence. The full sample of 62,521 star-forming galaxies is split into six equally populated bins, with each bin containing  $\sim 17,745$  galaxies. Within each redshift bin, the galaxies are split into 30 equally populated bins of stellar mass. The median SFR in each mass bin is calculated and then fit to  $S = S_0 - \log [1 + (10^{\mathcal{M}}/10^{M_0})^{-\gamma}]$ , where  $S = \log(\text{SFR})$  and  $\mathcal{M} = \log(M_*)$ . Table columns are as follows: (1) redshift range of bin; (2) median redshift; (3) stellar mass limit of redshift bin; (4)  $S_0$ , the maximum value of  $S$ ; (5) turnover mass; (6) low-mass power-law slope; (7) reduced  $\chi^2$  of fit.

in  $\gamma$  to steeper slopes at earlier cosmic times would suggest that the SFR in the lowest stellar mass galaxies does not increase as much as in more massive systems.

#### 4.3. Separating Quiescent Galaxies

We have described the MS relationship between SFR and  $M_*$  for star-forming galaxies. However, possible misclassification

of galaxies as either “star-forming” or “quiescent” could drastically affect the trends we observe.

As described in Section 4, we remove galaxies that are considered quiescent from our sample using the selection  $M_{\text{NUV}} - M_r > 3(M_r - M_J) + 1$  and  $M_{\text{NUV}} - M_r > 3.1$  (Ilbert et al. 2013). This selection is shown in Figure 7, with the full mass-selected sample of COSMOS galaxies at  $0.2 < z < 1.3$  generally

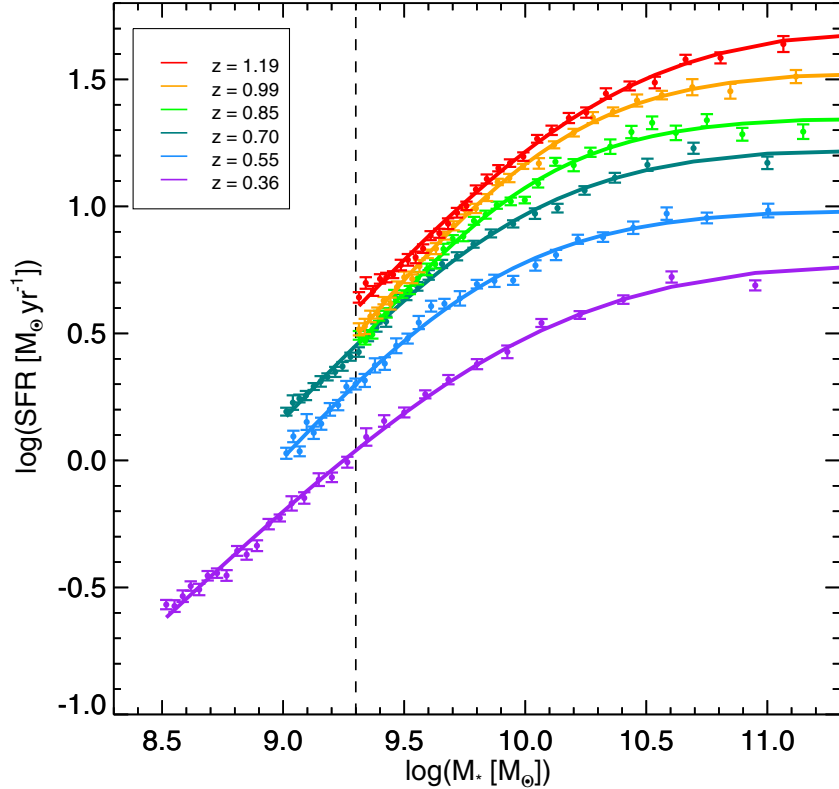


**Figure 5.** Median SFR in six equally populated redshift bins that have been split into 30 equally populated stellar mass bins. Errors on the median are calculated from bootstrapping. Solid lines represent the best-fit curve to the model  $S = S_0 - \log[1 + (10^M/10^{M_0})^{-\gamma}]$ . Vertical dashed line represents the stellar mass limit below which NRK has not been well calibrated.

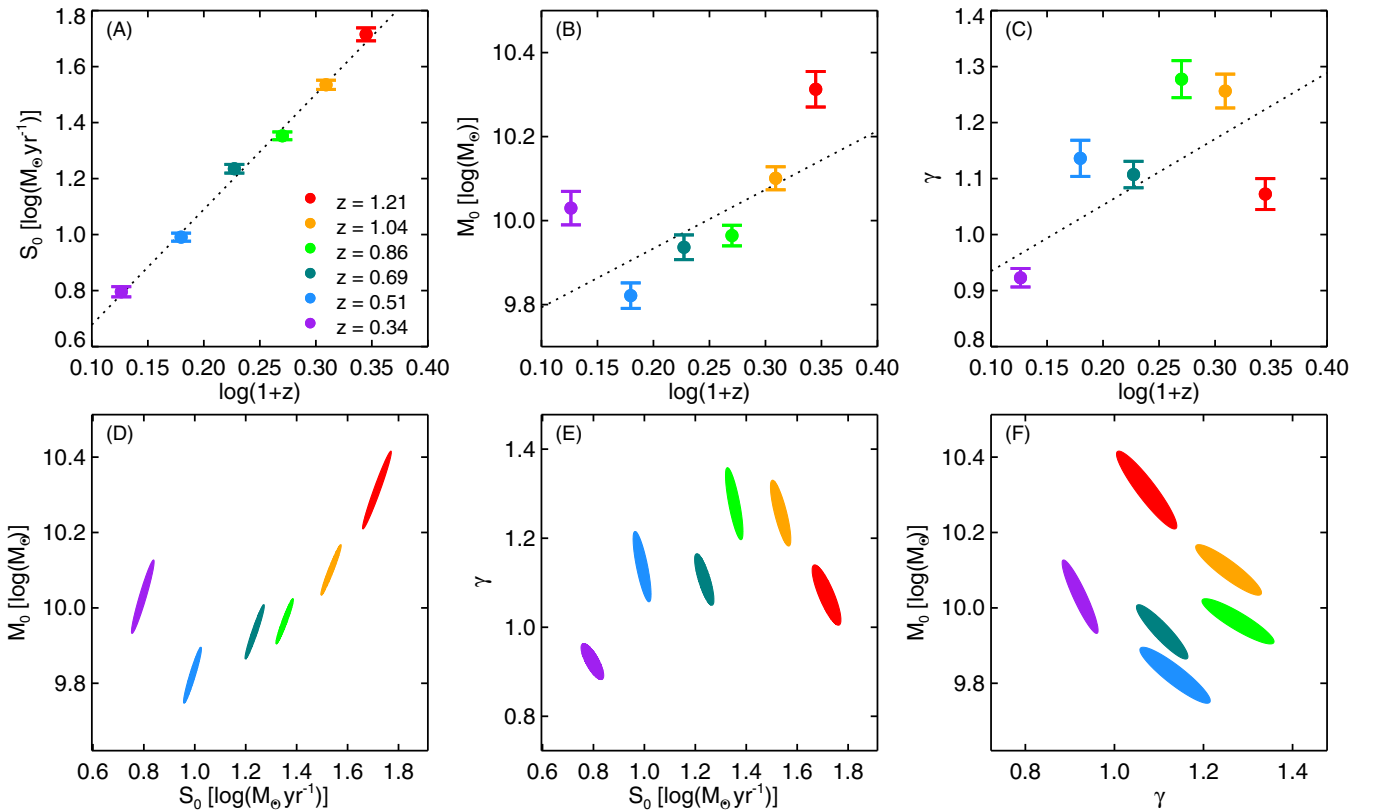


**Figure 6.** Top: redshift evolution of the best-fit parameter values for (A) maximum of  $\log(\text{SFR})$ ,  $S_0$ ; (B) turnover mass,  $M_0$ ; and (C) power-law slope,  $\gamma$ . Different color dots represent parameter values in different redshift bins with  $1\sigma$  error bars, and the dotted line is the best-fit linear fit to the data. Bottom: 95% confidence error ellipses displaying the covariance between (D)  $S_0$  and  $M_0$ ; (E)  $S_0$  and  $\gamma$ ; and (F)  $\gamma$  and  $M_0$ , with different colors once again representing different redshift bins. We see moderate covariance in  $\gamma$  and  $M_0$ , but little covariance between the other pairs.

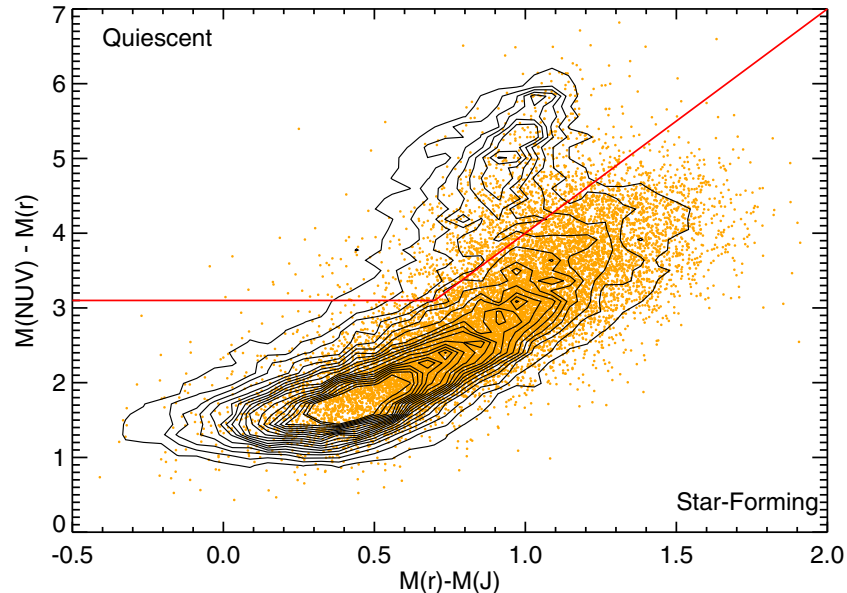


**Figure 7.**  $\text{NUV} - r^+$  vs.  $r^+ - J$  plot of a mass-selected sample of galaxies in COSMOS at  $0.2 < z < 1.3$ . Black contours represent the full sample of galaxies, while orange circles highlight galaxies that are IR-detected, either with *Herschel* or *Spitzer*  $24\ \mu\text{m}$ . The red line, from Ilbert et al. (2013), divides the sample into “star-forming” and “quiescent” galaxies. The majority of IR-detected galaxies are properly classified as “star forming,” but there is a significant population ( $\sim 7\%$ ) that are misclassified as “quiescent.”

separated into two distinct “star-forming” and “quiescent” regions. Improper classification of the “in between” galaxies that are not obviously star forming or quiescent could lead to changes in the MS shape. To test this possibility, we shift the entire separating line (both horizontal and diagonal segments) between quiescent and star-forming galaxies by  $\pm 0.4$  mag in  $M_{\text{NUV}} - M_r$ , and in either case there is no appreciable change to the MS.

Galaxies detected in the infrared by *Herschel* or *Spitzer*  $24\ \mu\text{m}$  are highlighted in Figure 7, and while the majority fall on the star-forming sequence, we see a number of objects that lie in the quiescent region. This population of infrared-detected quiescent (IR-Q) galaxies is relatively small, with only  $\sim 7\%$  of the galaxies classified as quiescent having detectable infrared emission, but these misclassified galaxies are predominantly found at high stellar mass. The fraction of quiescent galaxies detected in the infrared increases rapidly from  $\leq 1\%$  at  $M_* \sim 10^{9.5}\ M_\odot$  to  $15\%–20\%$  at  $M_* \geq 10^{11}\ M_\odot$ , and this trend holds at all redshifts. These massive galaxies could heavily influence the shape of the MS we observe, so it is vital to understand what is driving their infrared emission.

There could be several reasons why galaxies with quiescent colors have significant emission in the infrared, including (1) improper classification of star-forming galaxies possibly due to extreme dust obscuration, (2) elevated infrared luminosity from an AGN, (3) inaccurate absolute magnitudes due to catastrophic failures in photo- $z$ ’s or low signal-to-noise photometry, or (4) “post-starburst” infrared glow due to dust heating from young stars (that is not related to the instantaneous star formation).

AGNs typically heat dust to very hot temperatures, so we expect any AGN contribution to infrared radiation to be predominantly in near- and mid-IR wavelengths, while far-infrared emission is likely due to star formation alone. Only about 10% of the IR-Q galaxies have been detected by *Herschel*, and the rest are  $24\ \mu\text{m}$  only detections, where AGNs may heavily influence the emission. However, only  $\sim 1\%–5\%$  of the IR-Q galaxies are detected in the X-ray by *Chandra*, and

only  $\sim 2\%–8\%$  of the IR-Q galaxies have IRAC power-law colors indicative of AGNs, with significant overlap in those two populations, and the percentages are even lower when looking only at the  $24\ \mu\text{m}$  only sources. This suggests that radiation from an AGN is not fueling the infrared emission. The average SFR of the IR-Q galaxies with AGNs is 0.2–0.5 dex higher than the average SFR of all the IR-Q galaxies, so the presence of AGNs in these galaxies is likely just a reflection of the well-studied trend that AGN fraction increases with SFR or  $L_{\text{IR}}$  (e.g., Kartaltepe et al. 2010).

The rather high SFRs of the IR-Q galaxies suggest that they are indeed driven by star formation, and have been misclassified as quiescent. Man et al. (in preparation) stack the infrared emission from quiescent galaxies and find upper limits of  $\text{SFR}_{\text{IR}} < 0.1\text{--}1\ M_\odot\ \text{yr}^{-1}$ . The SFRs of the IR-Q galaxies in our sample tend to lie below the MS, but are all at least a factor of two to three higher than the upper limit from Man et al. (2014), which suggests that they are indeed still actively star forming. In addition, the infrared emission from IR-Qs is brighter than expected from a “post-starburst” glow (Hayward et al. 2014). It is unlikely that catastrophic photo- $z$  errors or low signal-to-noise photometry are causing these misidentifications, as the sources have excellent photometry and well-constrained photometric redshifts (only 0.1% of the IR-Q galaxies have  $\sigma_{\Delta z/(1+z)} > 0.15$ ). Thus, the likely explanation for these sources is that they are actively star-forming galaxies that have been misclassified as “quiescent,” and we include them in our analysis of the MS. We note, however, that the shape of the MS does not change significantly based on the inclusion or exclusion of these sources.

## 5. DISCUSSION

We see that the slope of the MS relationship between SFR and  $M_*$  changes with stellar mass. While most previous studies found a constant MS slope (for a summary see Speagle et al. 2014), some recent studies found a curved relationship might provide a better fit to the data (Karim et al. 2011; Whitaker et al.

2012). However, the mass completeness limit in both studies coincided with the turnover mass, leaving doubt as to whether the turnover was a real trend or an artifact of completeness. Salim et al. (2007) find that local star-forming galaxies follow a sequence best described by a piecewise linear fit. With our new COSMOS observations, we are able to study high redshift star-forming galaxies considerably less massive than the turnover mass, and we find that a single power law does not provide the best description of the star-forming MS.

### 5.1. The Turnover in the Star-forming Main Sequence

The relationship between SFR and  $M_*$  varies with stellar mass, with two distinct regions below and above the characteristic turnover mass,  $\mathcal{M}_0$ . What causes this change, and why does the turnover occur at about  $M_* \approx 10^{10} M_\odot$  at all redshifts?

#### 5.1.1. The Slope of the Main Sequence

The parameterization of the MS we employ in Section 4.1 includes a parameter  $\gamma$  that we describe as the low stellar mass power-law slope. However, we note that this slope is not derived from an actual power-law fit to the data, but instead represents the power-law slope that the relationship approaches in the very low-mass regime, based on Equation (2). This slope is significantly steeper than power-law slopes commonly quoted in the literature, and should not be compared to slopes from power-law fits to data.

For an easier comparison to the existing literature, we derive best-fit power-law relationships, fitting the low mass regime and high mass regime separately. Galaxies less massive than the turnover mass follow a fairly tight power-law relationship of  $SFR \propto M^\beta$ , with  $\beta = 0.88 \pm 0.06$ . This slope is shallower than  $\gamma$  because it includes galaxies in the “turnover region,” where the slope is already starting to flatten. Galaxies more massive than the turnover mass follow a drastically different relationship, with  $\beta = 0.27 \pm 0.04$  for  $M_* > 10^{10} M_\odot$ . A galaxy’s specific star formation rate ( $SSFR \equiv SFR/M_*$ ) can be interpreted as a measure of the efficiency of current star formation as compared to its past average star formation history. The SSFR of massive galaxies is systematically lower than would be expected from an extrapolation of low mass galaxies, suggesting that there may be decreased star formation efficiency in high stellar mass galaxies.

#### 5.1.2. Quenching in High Mass Galaxies

The turnover in the MS to lower star formation efficiencies in massive galaxies suggests there is a fundamental change that occurs as galaxies become more massive, as has been predicted in some studies. Galaxy luminosity and mass functions, which measure the brightness and mass distribution of galaxies at various lookback times, show a steep, exponential decline at high stellar masses and high luminosities while retaining a remarkably consistent shape at all redshifts (e.g., Bell et al. 2003; Pozzetti et al. 2010; Ilbert et al. 2013). The lack of large, bright galaxies throughout cosmic time argues for the presence of a characteristic mass above which a galaxy is likely to have its star formation strongly suppressed or quenched, and the evolution of galaxy mass functions demands a multi-slope MS with a shallower slope at high stellar masses (Leja et al. 2015).

In contrast, the dark matter halo mass function from semi-analytic models does not show the same exponential decline, and instead has a much shallower power-law cutoff at much higher masses (Somerville & Primack 1999; Benson et al. 2003),

leading to a “pivot mass” above which the ratio of dark matter to light matter increases rapidly (e.g., Leauthaud et al. 2012). At low stellar masses, the stellar to halo mass relation ( $M_h \propto M_*^{0.46}$ ; Leauthaud et al. 2012) and the dark matter halo growth rates from  $N$ -body simulations ( $\dot{M}_{\text{halo}} \propto (M_{\text{halo}})^{1.1}$ ; Wechsler et al. 2002; McBride et al. 2009; Fakhouri & Ma 2010) suggest a MS relationship of  $SFR \propto M_*^{1.04}$ , similar to the slope seen in the MS. The “pivot mass,” above which the stellar-to-halo mass relation deviates from the low stellar mass relationship, appears to evolve to higher  $M_*$  at higher redshifts (Leauthaud et al. 2012), at a rate similar to the possible evolution seen in the MS turnover mass,  $\mathcal{M}_0$ . In galaxies more massive than the “pivot mass,” the halo mass rises sharply in comparison with stellar mass, suggesting that while massive dark matter haloes appear to continue growing, the galaxies residing in them quench their star formation.

Possible mechanisms for this quenching include structural disruptions or galaxy mergers (Sanders & Mirabel 1996; Hopkins et al. 2006), feedback from accretion onto a supermassive black hole (Springel et al. 2005), gravitational heating of the surrounding intracluster medium (Khochfar & Ostriker 2008), changes in the mode of gas accretion onto galaxies (Kereš et al. 2005; Birnboim et al. 2007; Nelson et al. 2013), or gas removal or strangulation in dense environments (Peng et al. 2010, 2012).

Morphological studies may be key for understanding the star formation in massive galaxies. Abramson et al. (2014) find that galaxy SFRs are more strongly correlated to disk stellar mass (as opposed to total stellar mass), and that  $SSFR_{\text{disk}}$  is approximately constant with mass. If this is the case, the turnover in the MS could be simply due to growing bulges in the highest mass systems. However, one might expect the turnover to disappear (or become less severe) at high redshifts as galaxies become more disk-dominated, but this is not seen in the data. Schawinski et al. (2014) find that disk galaxies and elliptical galaxies likely quench their star formation rates through different processes with very different timescales. A galaxy’s physical size may also play a role in quenching, as the surface mass density has been shown to correlate strongly with SSFR (Kauffmann et al. 2003; Franx et al. 2008), and compact star forming galaxies may be on the evolutionary path toward quiescent galaxies (Barro et al. 2014).

Our data suggest that galaxies with high stellar mass ( $M_* > 10^{10} M_\odot$ ) are forming stars at a lower rate than would be expected from extrapolating the trends of low stellar mass galaxies. Finding the possible causes of this “quenching” of star formation is one of the key hurdles for understanding galaxy evolution. The existence of a turnover mass hints that the stellar mass of a galaxy plays a crucial role in quenching, possibly related to the “mass quenching” discussed in Peng et al. (2010). Further study is needed to determine the physical mechanism(s) behind quenching.

### 5.2. Increasing SFR with Redshift

From our fits, we find strong evolution in  $\mathcal{S}_0$ , which parameterizes the overall scaling of the  $SFR/M_*$  MS with redshift.<sup>15</sup> The scaling of the MS has been found in the literature to evolve as  $(1+z)^n$ , with the exponent  $n$  varying from  $2.2 < n < 5$  (Erb et al. 2006; Daddi et al. 2007; Damen et al. 2009; Dunne et al. 2009; Pannella et al. 2009; Karim et al. 2011). The value of  $n = 4.12 \pm 0.10$  we measure is among the steeper slopes seen in the literature.

<sup>15</sup> Alternatively, measuring the redshift evolution of the SFR at a constant characteristic mass provides similar results.

It's thought that the redshift evolution of the main-sequence normalization is due, at least in part, to increasing gas content in galaxies at earlier cosmic times. However, measuring the gas content in galaxies can be difficult, especially in high redshift systems. Molecular hydrogen is notoriously difficult to detect, so many surveys instead probe the rotational transitions of CO and use locally calibrated CO-to-H<sub>2</sub> conversion factors, although this conversion factor may differ in starburst galaxies (Tacconi et al. 2008; Magdis et al. 2011; Magnelli et al. 2012). Another method to estimate gas content is to measure the dust mass from far-infrared or submillimeter photometry and convert to gas masses using an assumed gas-to-dust ratio (e.g., Magdis et al. 2012; Santini et al. 2014; Scoville et al. 2014). Magdis et al. (2012) find gas fraction evolves as  $(1+z)^{2.8}$ , while recent ALMA observations suggest a steeper evolution of  $(1+z)^{5.9}$  (Scoville et al. 2014). Zahid et al. (2014) study the mass metallicity relationship and infer a much shallower evolution of gas mass  $M_g \propto (1+z)^{1.35}$ . Future studies will be needed to determine if the evolving normalization of the MS can be explained simply by an increasing gas supply in galaxies, or if other explanations such as increased merger rates or increased star formation efficiency are necessary to fully explain the observed evolution.

## 6. CONCLUSIONS

Using new far-infrared data from *Herschel*, we compare direct measurements of unobscured and obscured SFR with various SFR indicators that estimate the obscured SFR from data at shorter wavelengths (usually in optical or UV), and find that the NRK method of Arnouts et al. (2013) provides the most consistent estimate of the far-infrared derived SFR. By combining the SFRs from *Herschel*, *Spitzer*, and NRK, we analyze the relationship between SFR and  $M_*$  (commonly referred to as the “star-forming main sequence”) in 62,521 star-forming galaxies at  $z \leq 1.3$  in the COSMOS field. From our new analysis we find the following

1. The relationship between SFR and stellar mass does not follow a simple power law, but flattens to near-constant SFRs at high stellar masses. The shape of the MS is roughly constant for all redshifts  $z \leq 1.3$ .
2. The scaling of the entire star-forming MS rises with redshift as  $(1+z)^{4.12 \pm 0.10}$ .
3. The characteristic turnover mass lies at  $M_0 \approx 10^{10} M_\odot$ , with possible evolution toward higher turnover masses at high redshift.
4. The slope of the low-mass power law lies between  $\gamma = 0.9\text{--}1.3$ , with possible weak evolution toward steeper slopes at higher redshift.
5. A broken power-law fit to galaxies below and above the turnover mass results in  $\text{SFR} \propto M_*^{0.88 \pm 0.06}$  below the turnover mass and  $\text{SFR} \propto M_*^{0.27 \pm 0.04}$  above the turnover mass.

Our analysis suggests that star-forming galaxies cannot be described by a single power-law relationship between SFR and  $M_*$ , as had been suggested in many previous studies. Because of the strong effects of dust, direct observations in the FIR are crucial for studying the entire population of star-forming galaxies. In future work we will explore possible causes of the turnover in the MS by studying detailed morphology and examining possible feedback mechanisms, and we will extend our analysis to higher redshifts.

D.B.S. and C.M.C. acknowledge the hospitality of the Aspen Center for Physics, which is supported by the National Science Foundation grant No. PHY-1066293. C.M.C. acknowledges generous support from a McCue Fellowship through the University of California, Irvine's Center for Cosmology. K.S. gratefully acknowledges support from Swiss National Science Foundation Grant PP00P2\_138979/1. K.S. acknowledges support from the National Radio Astronomy Observatory, which is a facility of the National Science Foundation operated under cooperative agreement by Associated Universities, Inc.

COSMOS is based on observations with the NASA/ESA *Hubble Space Telescope*, obtained at the Space Telescope Science Institute, which is operated by AURA Inc, under NASA contract NAS 5-26555; also based on data collected at: the Subaru Telescope, which is operated by the National Astronomical Observatory of Japan; the *XMM-Newton*, an ESA science mission with instruments and contributions directly funded by ESA Member States and NASA; the European Southern Observatory, Chile; Kitt Peak National Observatory, Cerro Tololo Inter-American Observatory, and the National Optical Astronomy Observatory, which are operated by the Association of Universities for Research in Astronomy, Inc. (AURA) under cooperative agreement with the National Science Foundation; the National Radio Astronomy Observatory which is a facility of the National Science Foundation operated under cooperative agreement by Associated Universities, Inc; and the Canada–France–Hawaii Telescope operated by the National Research Council of Canada, the Centre National de la Recherche Scientifique de France and the University of Hawaii.

The Dark Cosmology Centre is funded by the Danish National Research Foundation.

## REFERENCES

- Abramson, L. E., Kelson, D. D., Dressler, A., et al. 2014, *ApJL*, 785, L36  
 Arnouts, S., Le Floc'h, E., Chevallard, J., et al. 2013, *A&A*, 558, A67  
 Barro, G., Faber, S. M., Pérez-González, P. G., et al. 2014, *ApJ*, 791, 52  
 Bell, E. F., McIntosh, D. H., Katz, N., & Weinberg, M. D. 2003, *ApJS*, 149, 289  
 Benson, A. J., Bower, R. G., Frenk, C. S., et al. 2003, *ApJ*, 599, 38  
 Birnboim, Y., Dekel, A., & Neistein, E. 2007, *MNRAS*, 380, 339  
 Brusa, M., Civano, F., Comastri, A., et al. 2010, *ApJ*, 716, 348  
 Bruzual, G., & Charlot, S. 2003, *MNRAS*, 344, 1000  
 Calzetti, D., Armus, L., Bohlin, R. C., et al. 2000, *ApJ*, 533, 682  
 Capak, P., Aussel, H., Ajiki, M., et al. 2007, *ApJS*, 172, 99  
 Casey, C. M. 2012, *MNRAS*, 425, 3094  
 Casey, C. M., Scoville, N. Z., Sanders, D. B., et al. 2014, *ApJ*, 796, 95  
 Chabrier, G. 2003, *PASP*, 115, 763  
 Chary, R., & Elbaz, D. 2001, *ApJ*, 556, 562  
 Civano, F., Brusa, M., Comastri, A., et al. 2011, *ApJ*, 741, 91  
 Condon, J. J. 1992, *ARA&A*, 30, 575  
 Daddi, E., Cimatti, A., Renzini, A., et al. 2004, *ApJ*, 617, 746  
 Daddi, E., Dickinson, M., Morrison, G., et al. 2007, *ApJ*, 670, 156  
 Dale, D. A., & Helou, G. 2002, *ApJ*, 576, 159  
 Damen, M., Labb  , I., Franx, M., et al. 2009, *ApJ*, 690, 937  
 Donley, J. L., Rieke, G. H., Pérez-Gonz  lez, P. G., et al. 2008, *ApJ*, 687, 111  
 Dunne, L., Ivison, R. J., Maddox, S., et al. 2009, *MNRAS*, 394, 3  
 Elbaz, D., Daddi, E., Le Borgne, D., et al. 2007, *A&A*, 468, 33  
 Elbaz, D., Dickinson, M., Hwang, H. S., et al. 2011, *A&A*, 533, A119  
 Erb, D. K., Steidel, C. C., Shapley, A. E., et al. 2006, *ApJ*, 647, 128  
 Fakhouri, O., & Ma, C.-P. 2010, *MNRAS*, 401, 2245  
 Franx, M., van Dokkum, P. G., Schreiber, N. M. F., et al. 2008, *ApJ*, 688, 770  
 Hayward, C. C., Lanz, L., Ashby, M. L. N., et al. 2014, *MNRAS*, 445, 1598  
 Helou, G., Soifer, B. T., & Rowan-Robinson, M. 1985, *ApJL*, 298, L7  
 Hinshaw, G., Larson, D., Komatsu, E., et al. 2013, *ApJS*, 208, 19  
 Hopkins, P. F., Hernquist, L., Cox, T. J., et al. 2006, *ApJS*, 163, 1  
 Ilbert, O., McCracken, H. J., Le F  vre, O., et al. 2013, *A&A*, 556, A55  
 Karim, A., Schinnerer, E., Mart  nez-Sansigre, A., et al. 2011, *ApJ*, 730, 61  
 Kartaltepe, J. S., Sanders, D. B., Le Floc'h, E., et al. 2010, *ApJ*, 709, 572  
 Kashino, D., Silverman, J. D., Rodighiero, G., et al. 2013, *ApJL*, 777, L8

- Kauffmann, G., Heckman, T. M., White, S. D. M., et al. 2003, *MNRAS*, **341**, 54
- Kennicutt, R. C., Jr. 1998, *ARA&A*, **36**, 189
- Kennicutt, R. C., Jr., Hao, C.-N., Calzetti, D., et al. 2009, *ApJ*, **703**, 1672
- Kereš, D., Katz, N., Weinberg, D. H., & Davé, R. 2005, *MNRAS*, **363**, 2
- Khochfar, S., & Ostriker, J. P. 2008, *ApJ*, **680**, 54
- Leauthaud, A., Tinker, J., Bundy, K., et al. 2012, *ApJ*, **744**, 159
- Lee, K.-S., Dey, A., Reddy, N., et al. 2011, *ApJ*, **733**, 99
- Lee, N., Le Floc'h, E., Sanders, D. B., et al. 2010, *ApJ*, **717**, 175
- Lee, N., Sanders, D. B., Casey, C. M., et al. 2013, *ApJ*, **778**, 131
- Le Floc'h, E., Aussel, H., Ilbert, O., et al. 2009, *ApJ*, **703**, 222
- Leja, J., van Dokkum, P. G., Franx, M., & Whitaker, K. E. 2015, *ApJ*, **798**, 115
- Lemaux, B. C., Le Floc'h, E., Le Fèvre, O., et al. 2014, *A&A*, **572**, 90
- Magdis, G. E., Daddi, E., Béthermin, M., et al. 2012, *ApJ*, **760**, 6
- Magdis, G. E., Daddi, E., Elbaz, D., et al. 2011, *ApJL*, **740**, L15
- Magnelli, B., Lutz, D., Saintonge, A., et al. 2014, *A&A*, **561**, A86
- Magnelli, B., Saintonge, A., Lutz, D., et al. 2012, *A&A*, **548**, A22
- Man, A. W. S., Greve, T. R., Toft, S., et al. 2014, *arXiv:1411.2870*
- Markwardt, C. B. 2009, in ASP Conf. Ser. 411, Astronomical Data Analysis Software and Systems XVIII, ed. D. A. Bohlender, D. Durand, & P. Dowler (San Francisco, CA: ASP), 251
- McBride, J., Fakhouri, O., & Ma, C.-P. 2009, *MNRAS*, **398**, 1858
- McCracken, H. J., Milvang-Jensen, B., Dunlop, J., et al. 2012, *A&A*, **544**, A156
- Meurer, G. R., Heckman, T. M., & Calzetti, D. 1999, *ApJ*, **521**, 64
- Murphy, E. J., Condon, J. J., Schinnerer, E., et al. 2011, *ApJ*, **737**, 67
- Nelson, D., Vogelsberger, M., Genel, S., et al. 2013, *MNRAS*, **429**, 3353
- Noeske, K. G., Weiner, B. J., Faber, S. M., et al. 2007, *ApJL*, **660**, L43
- Oteo, I., Cepa, J., Bongiovanni, Á., et al. 2013a, *A&A*, **554**, L3
- Oteo, I., Magdis, G., Bongiovanni, Á., et al. 2013b, *MNRAS*, **435**, 158
- Pannella, M., Carilli, C. L., Daddi, E., et al. 2009, *ApJL*, **698**, L116
- Papovich, C., Rudnick, G., Le Floc'h, E., et al. 2007, *ApJ*, **668**, 45
- Peng, Y.-J., Lilly, S. J., Kováč, K., et al. 2010, *ApJ*, **721**, 193
- Peng, Y.-J., Lilly, S. J., Renzini, A., & Carollo, M. 2012, *ApJ*, **757**, 4
- Pozzetti, L., Bolzonella, M., Zucca, E., et al. 2010, *A&A*, **523**, A13
- Rieke, G. H., Alonso-Herrero, A., Weiner, B. J., et al. 2009, *ApJ*, **692**, 556
- Rodighiero, G., Daddi, E., Baronchelli, I., et al. 2011, *ApJL*, **739**, L40
- Rodighiero, G., Renzini, A., Daddi, E., et al. 2014, *MNRAS*, **443**, 19
- Rujopakarn, W., Rieke, G. H., Weiner, B. J., et al. 2013, *ApJ*, **767**, 73
- Salim, S., Rich, R. M., Charlot, S., et al. 2007, *ApJS*, **173**, 267
- Sanders, D. B., & Mirabel, I. F. 1996, *ARA&A*, **34**, 749
- Santini, P., Maiolino, R., Magnelli, B., et al. 2014, *A&A*, **562**, A30
- Sargent, M. T., Béthermin, M., Daddi, E., et al. 2012, *ApJL*, **747**, L31
- Schawinski, K., Urry, C. M., Simmons, B. D., et al. 2014, *MNRAS*, **440**, 889
- Schreiber, C., Pannella, M., Elbaz, D., et al. 2014, *arXiv:1409.5433*
- Scoville, N., Aussel, H., Brusa, M., et al. 2007, *ApJS*, **172**, 1
- Scoville, N., Aussel, H., Sheth, K., et al. 2014, *ApJ*, **783**, 84
- Smail, I., Chapman, S. C., Blain, A. W., & Ivison, R. J. 2004, *ApJ*, **616**, 71
- Sobral, D., Best, P. N., Matsuda, Y., et al. 2012, *MNRAS*, **420**, 1926
- Somerville, R. S., & Primack, J. R. 1999, *MNRAS*, **310**, 1087
- Speagle, J. S., Steinhardt, C. L., Capak, P. L., & Silverman, J. D. 2014, *ApJS*, **214**, 15
- Springel, V., Di Matteo, T., & Hernquist, L. 2005, *ApJL*, **620**, L79
- Steinhardt, C. L., Speagle, J. S., Capak, P., et al. 2014, *ApJL*, **791**, L25
- Tacconi, L. J., Genzel, R., Smail, I., et al. 2008, *ApJ*, **680**, 246
- U, V., Sanders, D. B., Mazzarella, J. M., et al. 2012, *ApJS*, **203**, 9
- Wechsler, R. H., Bullock, J. S., Primack, J. R., et al. 2002, *ApJ*, **568**, 52
- Whitaker, K. E., Franx, M., Leja, J., et al. 2014, *ApJ*, **795**, 104
- Whitaker, K. E., van Dokkum, P. G., Brammer, G., & Franx, M. 2012, *ApJL*, **754**, L29
- Williams, R. J., Quadri, R. F., Franx, M., van Dokkum, P., & Labb  , I. 2009, *ApJ*, **691**, 1879
- Wuyts, S., F  rster Schreiber, N. M., Lutz, D., et al. 2011, *ApJ*, **738**, 106
- Yun, M. S., Reddy, N. A., & Condon, J. J. 2001, *ApJ*, **554**, 803
- Zahid, H. J., Dima, G. I., Kewley, L. J., et al. 2012, *ApJ*, **757**, 54
- Zahid, H. J., Dima, G. I., Kudritzki, R.-P., et al. 2014, *ApJ*, **791**, 130
- Zamojski, M. A., Schiminovich, D., Rich, R. M., et al. 2007, *ApJS*, **172**, 468